Nanoscale

PAPER

View Article Online
View Journal | View Issue

Cite this: *Nanoscale*, 2015, **7**, 6278

Velocity valleys enable efficient capture and spatial sorting of nanoparticle-bound cancer cells†

Justin D. Besant,[a] Reza M. Mohamadi,[b] Peter M. Aldridge,[a] Yi Li,[b] Edward H. Sargent[c] and Shana O. Kelley*[a,b,d]

The development of strategies for isolating rare cells from complex matrices like blood is important for a wide variety of applications including the analysis of bloodborne cancer cells, infectious pathogens, and prenatal testing. Due to their high colloidal stability and surface-to-volume ratio, antibody-coated magnetic nanoparticles are excellent labels for cellular surface markers. Unfortunately, capture of nanoparticle-bound cells at practical flow rates is challenging due to the small volume, and thus low magnetic susceptibility, of magnetic nanoparticles. We have developed a means to capture nanoparticle-labeled cells using microstructures which create pockets of locally low linear velocity, termed velocity valleys. Cells that enter a velocity valley slow down momentarily, allowing the magnetic force to overcome the reduced drag force and trap the cells. Here, we describe a model for this mechanism of cell capture and use this model to guide the rational design of a device that efficiently captures rare cells and sorts them according to surface expression in complex matrices with greater than 10 000-fold specificity. By analysing the magnetic and drag forces on a cell, we calculate a threshold linear velocity for capture and relate this to the capture efficiency. We find that the addition of X-shaped microstructures enhances capture efficiency 5-fold compared to circular posts. By tuning the linear velocity, we capture cells with a 100-fold range of surface marker expression with near 100% efficiency and sort these cells into spatially distinct zones. By tuning the flow channel geometry, we reduce non-specific cell adhesion by 5-fold.

Received 3rd February 2015,
Accepted 5th March 2015

DOI: 10.1039/c5nr00797f

www.rsc.org/nanoscale

1. Introduction

Rapid and efficient capture of rare cells from complex matrices is a requirement for a wide variety of applications including the isolation of cancer cells from blood,[1] detecting fetal cells in maternal circulation,[2] and diagnosing viral and bacterial infections.[3] Quantitative monitoring of cancer cells in the bloodstream is a particularly attractive goal, as it would enable non-invasive sampling to track disease progression, potentially using a liquid biopsy rather than one extracted from a tumor.[4] One challenge related to the isolation and analysis of bloodborne cancer cells is that they are present at extremely low concentrations,[5] and large volumes must therefore be processed rapidly to ensure the capture of at least a single cell. Moreover, circulating tumor cells (CTCs) may be heterogeneous and understanding the distribution of surface marker expression of the component subpopulations would allow greater resolution and precision when monitoring disease progression. For example, recent studies have shown that certain subpopulations of tumour cells have greater metastatic potential.[6]

Recently, a variety of microfluidic systems for rapid and automated capture of cancer cells have been reported including devices for size-based selection,[7–12] immunoaffinity-based capture,[5,13–16] fluorescent sorting,[17] and magnetic capture of nano- or microparticle labelled cells.[18–21] Microfluidic devices offer several advantages over strategies that simply isolate cells in a tube. Microfluidic devices enable the concentration of rare cells into small volumes and facilitate automated processing and analysis of the sample. In many applications, it is advantageous for cells to be released after capture for downstream analysis. Systems in which the device is directly functionalized with a capture agent require an enzymatic step to cleave the cells from the capture antibodies. In comparison, cells captured by magnetic particles can be easily released by removing the permanent magnet or turning off an electromagnet.[22] As

[a]*Institute for Biomaterials and Biomedical Engineering, University of Toronto, Toronto, M5S 3M2, Canada. E-mail: shana.kelley@utoronto.ca*
[b]*Department of Pharmaceutical Science, Leslie Dan Faculty of Pharmacy, University of Toronto, Toronto, M5S 3M2, Canada*
[c]*Department of Electrical and Computer Engineering, Faculty of Engineering, University of Toronto, Toronto, M5S 3G4, Canada*
[d]*Department of Biochemistry, Faculty of Medicine, University of Toronto, Toronto, M5S 1A8, Canada*
†Electronic supplementary information (ESI) available. See DOI: 10.1039/c5nr00797f

magnetic capture is non-destructive, the viable cells may be recovered.

Antibody-labeled paramagnetic nanoparticles have several advantages over magnetic microparticles for efficient cell capture, since their high surface-to-volume ratios allow thousands of binding events per cell and rapid binding kinetics.[23] Magnetic nanoparticles also possess higher colloidal stability than magnetic microparticles.[24] However, due to their small size, magnetic nanoparticles have inherently low magnetic susceptibilities, a consideration which demands a combination of high magnetic field gradients[25] and low flow velocities in order to achieve successful trapping of the nanoparticles. Unfortunately, low flow velocities are incompatible with the requirement of rapid processing of large (milliliter) volumes necessary for rare cell capture.

We recently developed a strategy for efficient nanoparticle-mediated capture of subpopulations of cancer cells in spatially distinct zones by manipulating the drag force in a microfluidic device.[26] This approach was validated using samples collected from prostate cancer patients and was shown to be effective at separating CTC subpopulations within these samples. Here we provide a detailed description of the capture mechanism through simulations and we develop a model for cell capture. We optimize a suite of parameters including the device geometry to maximize capture efficiency. The efficient capture of cells with a broad spectrum of EpCAM expression levels is demonstrated by tuning the flow velocity while minimizing non-specific cell adhesion. Using our model and findings, we rationally design a novel strategy for efficient capture and sorting of subpopulations of nanoparticle-bound rare cells directly from complex matrices with 5-fold higher purity than the method previously described.[26]

2. Materials and methods

2.1. Simulations

Simulations were carried out using COMSOL Multiphysics. We simulated the spatial distribution of linear velocities of fluid flowing in various device designs. We simulated the spatial distribution of magnetic fields and calculated the corresponding magnetic forces acting on super paramagnetic nanoparticles for our device geometry. Details of the simulations are included in the ESI.†

2.2. Cell culture

VCaP cells (ATCC CRL-2876) were cultured in DMEM medium (ATCC 30-2002). SK-BR-3 cells (ATCC HTB-30) were cultured in McCoy's Medium Modified (ATCC 30-2007). MDA-MB-231 cells (ATCC HTB-26) were cultured in Leibovitz's L-15 medium (ATCC 30-2008). All media was supplemented with 10% FBS and cells were cultured at 37 °C and 5% CO_2 in T75 flasks. Cells were collected by treating with 0.25% w/v trypsin with 0.53 mM EDTA for 3 minutes.

2.3. Chip fabrication

Masters were fabricated on silicon substrates and were patterned in SU-8 3050 (Microchem, MA) using photolithography. PDMS (Dow Chemical, MI) replicas were poured on masters and baked at 67 °C for 45 minutes. PDMS replicas were attached to no. 1 glass coverslips using a 30 s plasma treatment and left to bond overnight. The chip was sandwiched between arrays of N52 NdFeB magnets (K&J Magnetics, PA, 1.5 mm by 8 mm) with alternating polarity. Devices were treated with 1% Pluronic in PBS for 1 hour.

2.4. Estimating the number of nanoparticles per cell

We used a previously established method for estimating the number of nanoparticles per cell.[27] Full details are provided in the ESI.†

2.5. Cell capture in blood

Cells were diluted to the appropriate concentration, spiked in 1 mL of whole blood, mixed with 40 μl of anti-EpCAM Nano-Beads (MACS) and incubated for 20 minutes. The blood was introduced into the device using a syringe pump. Next 200 μl PBS-EDTA at 0.6 ml h^{-1} was introduced to wash non-specific cells. To measure non-specific cell adhesion as a function of zone geometry, we fabricated two versions of the device in which sequential zones double in width and height. 1 mL of whole blood was incubated with 40 μl of nanoparticles for 20 min and injected into the device at 0.6 mL h^{-1}. 200 μl PBS-EDTA at 0.6 ml h^{-1} was introduced as a wash step. The numbers of white blood cells were counted as below.

2.6. Immunostaining and imaging

Captured cells were counted with the aid of fluorescence microscopy. Before staining, captured cells were fixed inside the chip using 100 μL of 4% formaldehyde, followed by 100 μL 0.2% Triton X-100 (Sigma-Aldrich) for permeabilization. For staining in blood, we used 100 μL of the following reagents: DAPI ProLong Gold reagent (Invitrogen, CA) to stain cell nuclei, CK APC (Genetex GTX80205) and Anti-CD45 AF 488 (Invitrogen MHCD4520) to stain white blood cells. Antibodies were prepared in 100 μl PBS with 1% BSA and chips were stained for 60 minutes at a flow rate of 0.1 ml h^{-1}. For experiments in PBS, we stained cancer cell nuclei using 100 μL of DAPI. After staining, chips were washed twice with 100 μL PBS, dried, and stored at 4 °C. Chips were imaged using a fluorescent microscope (Nikon) with an automated stage controller and CCD (Hamamatsu, Japan) and images were automatically acquired with NES Elements (Nikon). Cells were enumerated by overlaying the bright field, red fluorescent, green fluorescent and blue fluorescent images.

3. Results and discussion

In our velocity valley chip (VVC), a flow channel is sandwiched between arrays of magnets that generate a high field

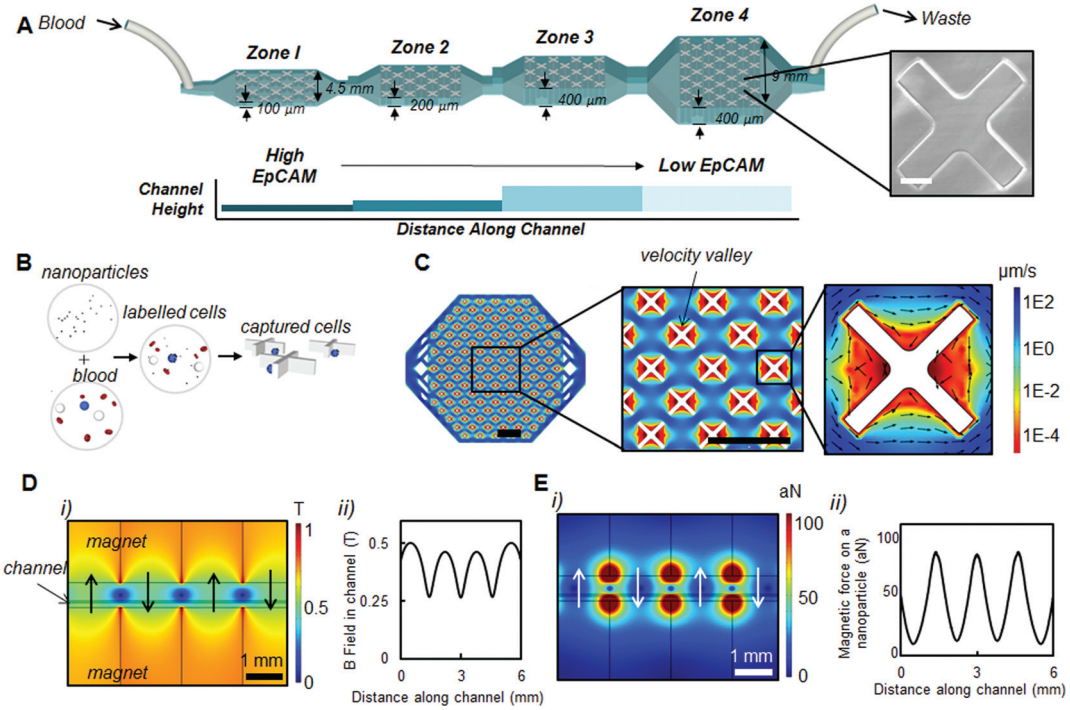

Fig. 1 The Velocity Valley Cell Capture Chip. (A) Schematic of the cell sorting device with 4 zones of decreasing average linear velocity. By increasing the channel cross section, the drag force drops by a factor of 2 in each sequential zone. Cells with high levels of surface markers are captured in the first zone while cells with low levels are captured in the final zone. The inset shows an optical microscopy image of a capture structure. The capture structures span the full height of the channel in each zone. The scale bar represents 150 μm. (B) Target cells are labelled with anti-EpCAM magnetic nanoparticles and introduced into the device. Target cells are captured by X-shaped capture structures. (C) Spatial distribution of linear velocities at 0.5 mL per hour in the first zone of the device. Velocity valleys are in red. Arrows represent normalized vectors. (D) (i) Magnetic field strength simulated in a cross section of the first zone of the chip. (ii) The strength of the magnetic fields as a function of channel length. (E) (i) Corresponding force on a single nanoparticle in the first zone of the device. As the force is proportional to the field gradient, it is highest at the magnet edges. (ii) The strength of the magnetic force acting on a single nanoparticle as a function of channel length. Scale bar represents 1 mm.

gradient inside the chip (Fig. 1A). Cells are labeled with magnetic nanoparticles coated with the epithelial cell adhesion marker (EpCAM), which is commonly overexpressed in a variety of cancers (Fig. 1B).[1,28] Key to this idea is the use of X-shaped capture structures (Fig. 1C) to generate regions of locally low flow velocity – which we term velocity valleys. Cells in the vicinity of a capture structure slow as they enter the velocity valley. While a cell is in the valley, the magnetic force is sufficient to overcome the lowered drag force. This enables efficient cell capture. Importantly, the structures do not trap non-target cells, and the device effectively captures cells with a wide range of surface marker expression levels.

To spatially sort cells based on surface marker expression, we designed a device with four zones in which the drag force decreases by a factor of 2 in each sequential zone (Fig. 1A). Cells bound by high numbers of nanoparticles are captured in the first zone with high linear velocities, while cells with lower numbers of bound nanoparticles are captured in the latter zones. The geometry of the zones are optimized to minimize device area which reduces non-specific cell adhesion and the time required to image the captured cells using fluorescence microscopy.

3.1. Optimization of capture structures

We sought to evaluate the performance of VVCs by simulating the distribution of linear velocities in devices with a variety of capture structure geometries (Fig. 2A). These capture structures span the full height of the channel. We calculated the percentage area of the device below a given linear velocity and plotted this as a cumulative distribution function (Fig. 2B). Given the same average input flow rate of 0.5 mL per hour, the percentage of the chip at low linear velocities is drastically increased when the 'X' shaped capture structures are present.

We hypothesized that these structures could allow for capture of nanoparticle-bound cells while maintaining a high average flow rate by increasing the percentage area of the chip with linear velocities below a threshold for capture (v_t). We define this threshold linear velocity as the velocity at which the corresponding drag force is lower than the magnetic force acting on the cell. Cells that enter a pocket of low velocity will slow down and experience a reduced drag force and thus, the relative ratio of the magnetic to drag forces will increase. If the cell is slowed below the threshold velocity, the magnetic force can overwhelm the drag force and the cell will be drawn to the

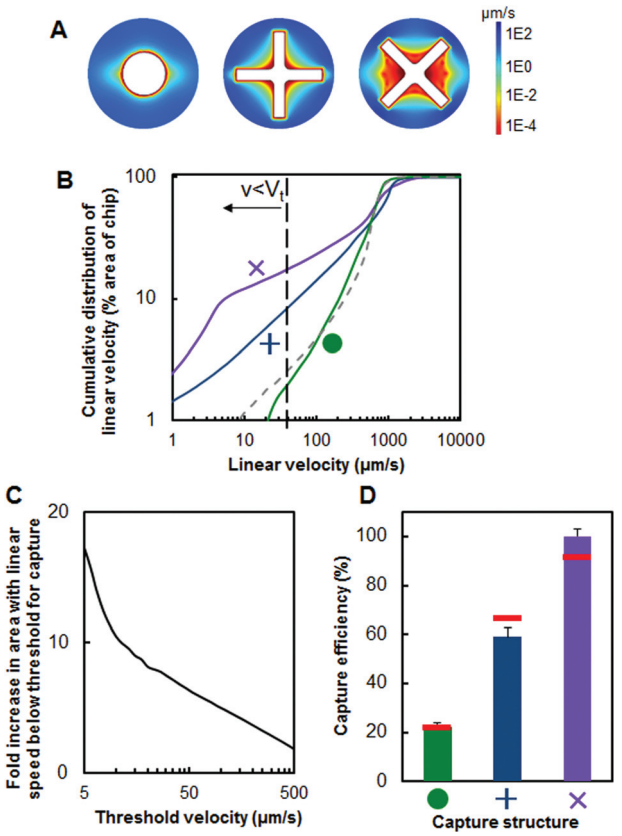

Fig. 2 Optimization of the capture structures. (A) Spatial distribution of linear velocities in devices with 'X', '+', and 'O' shaped structures. Velocity valleys are in red. (B) Cumulative distribution of linear velocities in devices with various capture structure geometries compared to a device without structures. The *y*-axis is the percent area of the chip with linear velocity less than or equal to the corresponding value on the *x*-axis. X-shaped capture structures markedly increase the percentage area of the chip with low linear velocities. (C) X-shaped capture structures drastically increase the area with linear speed below the threshold for capture when compared to circular posts which do not generate velocity valleys. (D) Capture efficiency as a function of capture structure geometry for VCaP cells. The red lines represent the predicted capture efficiency as a function of structure geometry. Error bars represent standard error.

chip walls where it will be trapped by a combination of magnetic, frictional, normal and adhesion forces.

Fig. 2C shows the increase in area of the chip over which the linear velocity lies below the threshold for capture. It compares a chip with 'X' shaped capture structures to a device with circular posts which do not generate velocity valleys. The 'X' shaped structures provide the greatest enhancement when the threshold velocity for capture is low. This corresponds to the case in which magnetic nanoparticles are employed, since they exhibit low magnetic susceptibility due to their small volume.

To verify the validity of our calculations, we fabricated devices with arrays of 'X', '+', and 'O' shaped capture structures. We challenged these devices with VCaP cells, a model prostate cancer cell line with a high level of EpCAM expression. VCaP cells were incubated with nanoparticles labelled with an anti-EpCAM antibody for 20 minutes and introduced into the device. Fig. 2D shows capture efficiency as a function of capture structure geometry. The X-shaped capture structures captured cells with 5× greater efficiency than circular posts. These results agree with the simulations of capture efficiency as outlined below as the posts do not create the low-velocity pockets necessary for effective capture of nanoparticle labeled cells. The capture efficiency of U937 cells, a cell line which does not express EpCAM, was less than 0.1% for all capture structure designs indicating that only cells tagged with magnetic particles will be captured.

3.2. Modelling the capture efficiency of a velocity valley chip

As a complement to our numerical simulations of the flow and magnetic fields generated by the magnet array, we analyzed the drag and magnetic forces acting on a cell to develop a predictive model for cell capture using the X-shaped structures. At low Reynolds numbers, drag on a cell is governed by Stokes' law:

$$F_d = 6\pi\eta r v \quad (1)$$

where F_d [N] is the drag force, r [m] is the cell or nanoparticle radius, η [Pa s] is the dynamic viscosity of the medium (0.001 Pa s), and v [m s^{-1}] is the relative velocity of the cell compared to the surrounding fluid.

The magnetic force acting on superparamagnetic nanoparticles is:[29]

$$\vec{F}_{m\_bead} = V_m \frac{\Delta\chi_{bead}}{\mu_0}(\vec{B}\cdot\nabla)\vec{B} \quad (2)$$

where V_m [m^3] is the nanoparticle volume, $\Delta\chi_{bead}$ [unitless] is the difference between the magnetic susceptibility of the nanoparticle and the medium, μ_0 [H m^{-1}] is the permeability of free space ($4\pi \times 10^{-7}$ H m^{-1}), and $\vec{B}$ [T] is the applied magnetic field. The magnetic force acting on a cell is given by multiplying the magnetic force on an individual nanoparticle by the average number of nanoparticles per cell (N_b):

$$\vec{F}_{m\_cell} = N_b V_m \frac{\Delta\chi_{bead}}{\mu_0}(\vec{B}\cdot\nabla)\vec{B} \quad (3)$$

Thousands of nanoparticles may bind to a cell[30] and the exact value of N_b depends on the cell type and the affinity constant of the antibodies. For the MACS 50 nm superparamagnetic nanoparticles, $V_m\Delta\chi_{bead}$ is 2.5×10^{-16} mm^3.[30,31] Since the magnetic fields vary within the channel as a function of distance along the channel and channel height (Fig. S1†) we use the maximum magnetic force acting on a cell in our calculations.

Predicting exactly where a cell will be captured in the chip is challenging. We sought to develop a model to analyze various device designs in order to quickly predict performance. Neglecting gravity, the cells will be subjected to several forces as they flow through the microfluidic chip: a drag force in the direction of the flow, a magnetic force in the transverse direction, and a drag force in the transverse direction which

opposes the magnetic force (Fig. S2†). However, once a cell is captured at one of the boundaries of the chip, friction, adhesion and normal forces are the dominant components keeping the cell fixed in place. In order to determine where the cells will most likely be brought into contact with the chip boundaries, it is useful to compare the relative magnitudes of the drag and magnetic forces acting on a cell. In regions of high flow velocity, the drag force in the direction of the flow will be much greater than the magnetic and transverse drag forces acting on the cell, leading to a resultant cell velocity which is essentially parallel to the flow streamlines. Conversely, in a velocity valley (where the flow velocity is low) the magnitude of the magnetic and transverse drag forces acting on the cell should match or exceed that of the drag force resulting from the flow, yielding a velocity vector which drives the cell towards the boundaries of the chip.

There is a high probability of cell capture if the magnitude of the magnetic force experienced by the cell is much greater than the magnitude of the drag force which opposes capture. Therefore, we define a threshold linear velocity, v_t, such that the corresponding drag force is equivalent to the maximum magnetic force acting on a cell inside the channel. Cells in an area of the chip with high local linear velocity (greater than v_t) are unlikely to be captured while those in area of low linear velocity (less than v_t) have a higher probability of capture. We approximate that the probability of cell capture at a given structure, $P_{capture}$, is proportional to $A_{V<v_t}$, the average percentage of area surrounding a capture structure in which the linear velocity is less than the threshold. As the time spent in proximity of a capture structure decreases linearly with increasing flow rate, we also assume the probability of cell capture at a given structure is inversely proportional to the flow rate.

The total capture efficiency, E, can be calculated as:

$$E = 100\% \ (1 - (1 - P_{capture})^N) \quad (4)$$

where N is the number of capture structures in each cell's path, $P_{capture}$ is the probability of capture at a capture structure, and $P_{capture} = \alpha \frac{A_{V<v_t}}{\dot{Q}}$ where $\dot{Q}$ is the flow rate (mL h^{-1}), and α is an experimentally determined proportionality constant (h mL^{-1}) with units set to ensure that $P_{capture}$ is unitless. A limitation of this model is that it does not account for the spatial overlay of the magnetic and drag forces. This model also does not account for the frictional and normal forces acting on the cell. Additional details of the model are provided in the ESI.†

3.3. Capture efficiency as a function of flow rate

Our initial tests were conducted with VCaP, a cell line with high expression of EpCAM; however, in other cell lines, EpCAM levels may vary over a wide range between 1×10^4 to 1×10^7 sites per cell.[32] To examine the performance of our device with a cell line with a moderate level of EpCAM expression, we chose to test SKBR3, a breast cancer cell line which has approximately 10-fold lower EpCAM expression than VCaP.[26] We measured the capture efficiency of SKBR3 cells as a function of volumetric flow rate (Fig. 3C). As expected, the capture efficiency increased with decreasing flow rate.

We used eqn (4) to model the capture efficiency as a function of flow rate for SKBR3 cells. First, we calculated the magnetic force acting on 50 nm nanoparticles using eqn (2) and found the maximum force on a magnetic nanobead is 143 aN (Fig. 1E). Next, we estimated the number of nanoparticles bound to SKBR3 cells by measuring the deflection of nanoparticle labelled cells flowing in a channel under the influence of a magnetic field (Fig. S3†), a method previously established by other authors.[27] The number of nanoparticles per cell can be calculated by measuring the transverse velocity in the channel and using it to calculate the corresponding Stokes drag force. By equating the Stokes drag force to the magnetic force, using eqn (3), it is possible to determine the number of nanoparticles per cell.

We validated the method using magnetic microparticles having known magnetic susceptibilities. Our results indicate that the ratio of the magnetic force to the Stokes drag force is approximately 1, indicating that our chosen measurement technique was valid (Fig. 3A).

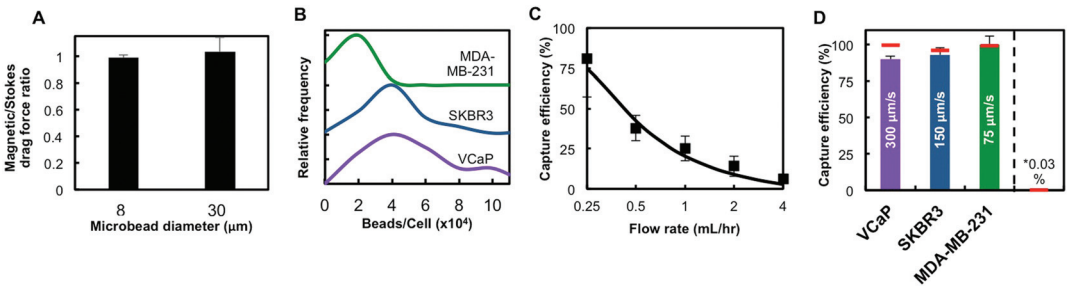

Fig. 3 Tuning the linear velocity to capture different cell types. (A) Validation of the method to measure the magnetic force using magnetic microbeads. These results validate the assumption that the Stokes drag force can be equated to the magnetic force. (B) Distribution of the number of nanoparticles per cell for three cell lines. (C) Capture efficiency as a function of flow rate for SKBR3 cells. The black line represents the predicted capture efficiency. (D) Capture efficiency as a function of cell type. By tuning the linear velocity it was possible to capture all three cell lines with greater than 90% efficiency. U937 cells, which do not express EpCAM, are captured with less than 0.1% efficiency. Less than 2% of cells were captured when magnets were removed. The red lines represent the predicted capture efficiency. Error bars represent standard error.

We found an average of 3.3×10^4 nanoparticles per cell for the SKBR3 cell line (Fig. 3B). This gives a maximum magnetic force per cell of 5 pN which corresponds to a threshold linear velocity for capture of 25 μm s^{-1}. Using eqn (4), we modeled the capture efficiency as a function of flow rate and fit our model to the capture efficiency data points (Fig. 3C). We found our model best fit the data when α, the experimentally determined proportionality factor, was 0.1. We also calculated the predicted capture efficiency as a function of structure geometry and found good agreement with our measured experimental capture results (Fig. 2D).

3.4. Tuning the flow rate to capture a wide range of cell types

We selected a suite of cell lines with a spectrum of EpCAM expression levels to evaluate how the VVC approach performed with varying surface marker levels. The cell lines selected were VCaP, SKBR3 and MDA-MB-231, three cancer lines which have high, moderate, and low levels of EpCAM respectively. VCaP express EpCAM at levels approximately 10-fold higher than SKBR3[26] which in turn express EpCAM 10-fold higher than MDA-MB-231.[21] Using the established method for measuring the number of nanoparticles per cell,[27] we generated a histogram of the number of beads per cell and found a broad distribution of beads per cell for each cell line. Using the mean numbers of nanoparticles from the histogram, we found an average of 4.3×10^4, 3.3×10^4, and 5×10^3 nanoparticles per cell for VCaP, SKBR3 and MDA-MB-231, respectively (Fig. 3B). Our calculations are in line with values previously reported in the literature.[30]

To study capture efficiency as a function of EpCAM expression, we challenged the VVC with each of these cell lines and measured the capture efficiency at various flow rates (Fig. 3D). We found that by tuning the flow rate we could capture all three cell lines with greater than 90% efficiency. As expected, lower flow rates were needed for efficient capture of MDA-MB-231 cells, which have low EpCAM expression, than VCaP cells, which express high levels of EpCAM. These results suggest that by tuning the flow rate, our device is capable of capturing a wide range of cell types.

We challenged the device with 1 000 000 U937 cells to evaluate the non-specific binding that might occur in a blood sample. U937 is a white blood cell line that does not express EpCAM. These cells were tested with a flow rate of 0.5 mL h^{-1} and the capture efficiency was less than 0.1% (Fig. 3D). These control experiments suggest the X-shaped structures only are capable of trapping cells when coupled with a magnetic force. We modelled the capture efficiency as a function of the number of bound nanoparticles and flow rate (Fig. 3D). We found good agreement between our model and the experimental capture efficiency.

3.5. Validation in complex matrices

To validate the performance of the VVC in complex matrices, we challenged our device with undiluted, whole blood. We spiked serial dilutions of VCaP cells in blood and incubated the cells with nanoparticles for 20 min. The whole blood was introduced into the device at 0.6 mL h^{-1}. After capture, cancer cells were distinguished from nucleated white blood cells using a series of fluorescent stains for cytokeratin (CK), an epithelial marker, CD-45, a pan-leukocyte marker, and DAPI, which stains the nucleus. Cancer cells were identified as DAPI+/CK+/CD45− and white blood cells were identified as DAPI+/CK−/CD45+ (Fig. 4A). The magnet must be removed prior to imaging which can dislocate the cells from the X-shaped structures (Fig. 4B).

VCaP cells were captured with high efficiency at all concentrations tested (Fig. 4C). VCaP cells were not identified in whole blood samples that did not contain spiked cells. In a given device, we would typically observe less than 200 white blood cells, which is less than 0.01% of the WBCs introduced, indicating the cancer cells are recovered with greater than 10 000-fold specificity.

3.6. Minimizing non-specific cell adhesion by tuning channel geometry

Motivated by results indicating that the cells with different surface marker expression are efficiently captured at different average linear velocities, we sought to design a device to spatially sort cells based on surface marker expression. We designed a device with multiple zones in which the linear velocity drops stepwise by a factor of 2 in each sequential zone. We hypothesized that cells with high surface marker expression and correspondingly high numbers of bound nanoparticles would be captured in the initial zones of high linear velocity while cells with low EpCAM expression would be captured in the latter zones with low linear velocity.

To study the effect of device geometry on non-specific cell adhesion, we devised two strategies to increase the channel cross-sectional area in successive zones to manipulate the average linear velocity. In the first approach, the channel height is held constant and the channel width doubles in successive zones. In the second approach, we hold the channel width constant while doubling the channel height.

We challenged both devices with 1 mL of undiluted blood at 0.6 mL h^{-1} and counted the number of non-specific cells bound to the device using fluorescence immuno-staining. Fig. 4D shows the number of non-specific white blood cells captured in each zone. We found that the numbers of non-specifically bound cells is approximately proportional to the zone width. In comparison, the number of non-specifically bound cells increases much more slowly as a function of zone height. In the latter zones, the number of non-specifically bound cells is 5-fold higher when successive zones increase in width rather than height. The increase in purity when successive zones increase in height is 1.9-fold, 2.1-fold, 5.3-fold and 5.2-fold in zones 1 through 4 respectively. This is expected as non-specific cell adhesion increases as a function of surface area and thus the propensity for non-specific cell adhesion increases in the wider zones. In comparison, as the channel is much wider than it is tall, the device surface area does not increase appreciably as a function of channel height (Table S5†) which minimizes non-specific cell adhesion.

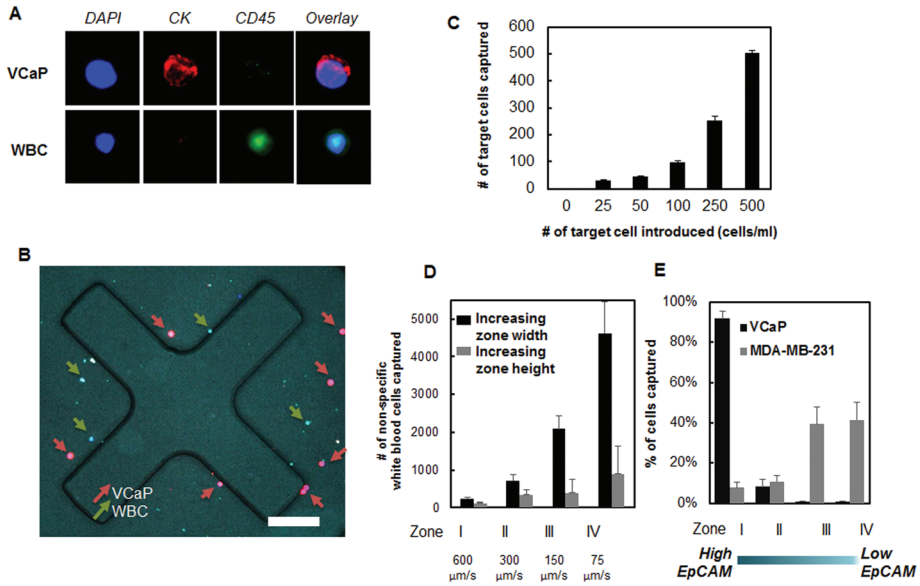

Fig. 4 Capture and sorting of rare cells in blood. (A) After capture, cancer cells are stained for DAPI, CK, and CD45. VCaP cells are identified as DAPI+/CK+/CD45– and nucleated white blood cells are identified as DAPI+/CK–/CD45+. (B) VCaP cells trapped near the vicinity of an X-shaped capture structure. The scale bar represents 150 μm. (C) Capture efficiency as a function of the number of VCaP cells spiked in whole, undiluted blood. Error bars represent standard error. (D) The number of non-specifically bound white blood cells (WBCs) across the 4 zones of the device when sequential zones double in height *vs.* width. (E) Distribution of two cell lines, VCaP and MDA-MB-231, with high and low EpCAM expression respectively across the 4 zones of the device. Whole blood was introduced into the device at 0.6 mL h^{-1}.

3.7. Sorting cells by surface marker expression

Motivated by our results, we designed a device to sort cells based on surface marker expression into four spatially distinct zones. This device consists of four zones in which the linear velocity drops by 2 in each successive zone (Fig. 1A). In the first three zones, the channel width is held constant while the height doubles. Due to limitations in fabricating features greater than 500 μm using photolithography, in the fourth zone, the channel height is held constant and the channel width increases. Although the channel height does increase in the latter zones, the magnetic fields do not decrease appreciably within the channel as the bottom magnet remains at a constant distance below the channel (Fig. S1†). We challenged the device with VCaP and MDA-MB-231 cells spiked in blood which have high and low expression of EpCAM respectively and measured the numbers of cells captured in each zone (Fig. 4E). We found that 92% of VCaP cells were captured in the first zone with highest average linear velocity while 82% of MDA-MB-231 cells were captured in the latter two zones with the lowest linear velocity.

These results suggest that this device could be used to spatially sort rare cells as a function of surface marker expression with high purity. Our results indicate that manipulating the linear velocity using a channel height increase can reduce the amount of non-specific binding by minimizing the device surface area. Combinations of increasing both the height and width of the device would expand the dynamic range of linear velocities. Another advantage of this device is that it minimizes the footprint which reduces the time required to image the device using fluorescence microscopy and decreases fabrication costs. By increasing the channel cross-section, it is possible to increase the average flow rate, and thus throughput, while maintaining the same in-channel linear velocity.

4. Conclusions

We elaborate the mechanisms, models, and optimization of a microfluidic device for the capture of rare cells in whole blood. This chip enables capture of cells bound by low magnetic susceptibility nanoparticles using capture structures which create velocity valleys, or zones of low-linear velocity. These structures tilt the balance of forces acting on a nanoparticle-bound cell in favour of the action of the magnetic force. Using X-shaped capture structures provides a 5-fold enhancement in capture efficiency over circular posts. By tuning the average flow rate, we efficiently capture cells with a 100-fold difference in EpCAM expression and sort these cells into spatially distinct zones. We optimize the device geometry to reduce non-specific cell adhesion by 5-fold and demonstrate that in whole blood, we successfully recover cancer cells with greater than 10 000-fold specificity. By changing the capture label on the magnetic nanoparticles, this strategy could be used for capture of a wide variety of rare cell types.

Acknowledgements

We thank the ECTI facility at the University of Toronto for their cleanroom facilities. We also thank the Ontario Research

Fund, the Natural Sciences and Engineering Council, and the Canadian Institutes for Health Research for grants that supported this work.

Notes and references

1 K. Pantel, R. H. Brakenhoff and B. Brandt, *Nat. Rev. Cancer*, 2008, **8**, 329–340.
2 D. M. Kavanagh, M. Kersaudy-Kerhoas, R. S. Dhariwal and M. P. Y. Desmulliez, *J. Chromatogr. B*, 2010, **22**, 1905–1911.
3 X. Cheng, D. Irimia, M. Dixon, K. Sekine, U. Demirci, L. Zamir, R. G. Tompkins, W. Rodriguez and M. Toner, *Lab Chip*, 2007, **7**, 170–178.
4 M. Cristofanilli, *Semin. Oncol.*, 2006, **33**, S9–14.
5 S. Nagrath, L. V. Sequist, S. Maheswaran, D. W. Bell, D. Irimia, L. Ulkus, M. R. Smith, E. L. Kwak, S. Digumarthy, A. Muzikansky, P. Ryan, U. J. Balis, R. G. Tompkins, D. a. Haber and M. Toner, *Nature*, 2007, **450**, 1235–1239.
6 I. Baccelli, A. Schneeweiss, S. Riethdorf, A. Stenzinger, A. Schillert, V. Vogel, C. Klein, M. Saini, T. Bäuerle, M. Wallwiener, T. Holland-Letz, T. Höfner, M. Sprick, M. Scharpff, F. Marmé, H. P. Sinn, K. Pantel, W. Weichert and A. Trumpp, *Nat. Biotechnol.*, 2013, **31**, 539–544.
7 S. Zheng, H. K. Lin, B. Lu, A. Williams, R. Datar, R. J. Cote and Y.-C. Tai, *Biomed. Microdevices*, 2011, **13**, 203–213.
8 H. K. Lin, S. Zheng, A. J. Williams, M. Balic, S. Groshen, H. I. Scher, M. Fleisher, W. Stadler, R. H. Datar, Y.-C. Tai and R. J. Cote, *Clin. Cancer Res.*, 2010, **16**, 5011–5018.
9 H. J. Lee, J. H. Oh, J. M. Oh, J.-M. Park, J.-G. Lee, M. S. Kim, Y. J. Kim, H. J. Kang, J. Jeong, S. Il Kim, S. S. Lee, J.-W. Choi and N. Huh, *Angew. Chem., Int. Ed.*, 2013, **52**, 8337–8340.
10 E. Sollier, D. E. Go, J. Che, D. R. Gossett, S. O'Byrne, W. M. Weaver, N. Kummer, M. Rettig, J. Goldman, N. Nickols, S. McCloskey, R. P. Kulkarni and D. Di Carlo, *Lab Chip*, 2014, **14**, 63–77.
11 J. H. Son, S. H. Lee, S. Hong, S. Park, J. Lee, A. M. Dickey and L. P. Lee, *Lab Chip*, 2014, **14**, 2287–2292.
12 H. J. Yoon, M. Kozminsky and S. Nagrath, *ACS Nano*, 2014, 1995–2017.
13 S. L. Stott, C.-H. Hsu, D. I. Tsukrov, M. Yu, D. T. Miyamoto, B. a. Waltman, S. M. Rothenberg, A. M. Shah, M. E. Smas, G. K. Korir, F. P. Floyd, A. J. Gilman, J. B. Lord, D. Winokur, S. Springer, D. Irimia, S. Nagrath, L. V. Sequist, R. J. Lee, K. J. Isselbacher, S. Maheswaran, D. a. Haber and M. Toner, *Proc. Natl. Acad. Sci. U. S. A.*, 2010, **107**, 18392–18397.
14 H. J. Yoon, T. H. Kim, Z. Zhang, E. Azizi, T. M. Pham, C. Paoletti, J. Lin, N. Ramnath, M. S. Wicha, D. F. Hayes, D. M. Simeone and S. Nagrath, *Nat. Nanotechnol.*, 2013, **8**, 735–741.
15 Y. Xu, J. A. Phillips, J. Yan, Q. Li, Z. H. Fan, W. Tan and P. O. Box, *Anal. Chem.*, 2009, **81**, 7436–7442.
16 V. Murlidhar, M. Zeinali, S. Grabauskiene, M. Ghannad-Rezaie, M. S. Wicha, D. M. Simeone, N. Ramnath, R. M. Reddy and S. Nagrath, *Small*, 2014, 4895–4904.
17 P. G. Schiro, M. Zhao, J. S. Kuo, K. M. Koehler, D. E. Sabath and D. T. Chiu, *Angew. Chem., Int. Ed.*, 2012, **51**, 4618–4622.
18 A.-E. Saliba, L. Saias, E. Psychari, N. Minc, D. Simon, F.-C. Bidard, C. Mathiot, J.-Y. Pierga, V. Fraisier, J. Salamero, V. Saada, F. Farace, P. Vielh, L. Malaquin and J.-L. Viovy, *Proc. Natl. Acad. Sci. U. S. A.*, 2010, **107**, 14524–14529.
19 K. Hoshino, Y.-Y. Huang, N. Lane, M. Huebschman, J. W. Uhr, E. P. Frenkel and X. Zhang, *Lab Chip*, 2011, **11**, 3449–3457.
20 J. H. Kang, S. Krause, H. Tobin, A. Mammoto, M. Kanapathipillai and D. E. Ingber, *Lab Chip*, 2012, **12**, 2175–2181.
21 E. Ozkumur, A. M. Shah, J. C. Ciciliano, B. L. Emmink, D. T. Miyamoto, E. Brachtel, M. Yu, P. Chen, B. Morgan, J. Trautwein, A. Kimura, S. Sengupta, S. L. Stott, N. M. Karabacak, T. a. Barber, J. R. Walsh, K. Smith, P. S. Spuhler, J. P. Sullivan, R. J. Lee, D. T. Ting, X. Luo, A. T. Shaw, A. Bardia, L. V. Sequist, D. N. Louis, S. Maheswaran, R. Kapur, D. a. Haber and M. Toner, *Sci. Transl. Med.*, 2013, **5**, 179ra47.
22 A. Hosseini and L. Soleymani, *Appl. Phys. Lett.*, 2014, **105**, 074102.
23 S. Miltenyi, W. Müller, W. Weichel and a. Radbruch, *Cytometry*, 1990, **11**, 231–238.
24 M. Colombo, S. Carregal-Romero, M. F. Casula, L. Gutiérrez, M. P. Morales, I. B. Böhm, J. T. Heverhagen, D. Prosperi and W. J. Parak, *Chem. Soc. Rev.*, 2012, **41**, 4306.
25 B. Teste, F. Malloggi, A.-L. Gassner, T. Georgelin, J.-M. Siaugue, A. Varenne, H. Girault and S. Descroix, *Lab Chip*, 2011, **11**, 833–840.
26 R. M. Mohamadi, J. D. Besant, A. Mepham, B. Green, L. Mahmoudian, T. Gibbs, I. Ivanov, A. Malvea, J. Stojcic, A. L. Allan, L. E. Lowes, E. H. Sargent, R. K. Nam and S. O. Kelley, *Angew. Chem., Int. Ed.*, 2015, **54**, 139–143.
27 K. S. Kim and J.-K. Park, *Lab Chip*, 2005, **5**, 657–664.
28 P. T. Went, A. Lugli, S. Meier, M. Bundi, M. Mirlacher, G. Sauter and S. Dirnhofer, *Hum. Pathol.*, 2004, **35**, 122–128.
29 S. S. Shevkoplyas, A. C. Siegel, R. M. Westervelt, M. G. Prentiss and G. M. Whitesides, *Lab Chip*, 2007, **7**, 1294–1302.
30 K. E. McCloskey, J. J. Chalmers and M. Zborowski, *Anal. Chem.*, 2003, **75**, 6868–6874.
31 H. Zhang, L. R. Moore, M. Zborowski, P. S. Williams, S. Margel and J. J. Chalmers, *Analyst*, 2005, **130**, 514–527.
32 N. Prang, S. Preithner, K. Brischwein, P. Göster, a. Wöppel, J. Müller, C. Steiger, M. Peters, P. a. Baeuerle and a. J. da Silva, *Br. J. Cancer*, 2005, **92**, 342–349.